The Astronomical Journal, 130:308–318, 2005 July
© 2005. The American Astronomical Society. All rights reserved. Printed in U.S.A.

ALBEDOS OF ASTEROIDS IN COMET-LIKE ORBITS

Yanga R. Fernández,[1] David C. Jewitt,[1] and Scott S. Sheppard[1,2]
Institute for Astronomy, University of Hawai'i at Mānoa, 2680 Woodlawn Drive, Honolulu, HI 96822;
yan@ifa.hawaii.edu, jewitt@hawaii.edu, sheppard@dtm.ciw.edu
Received 2005 January 30; accepted 2005 March 24

ABSTRACT

We present the results of a mid-infrared survey of 26 asteroids in comet-like orbits, including six Damocloids and six near-Earth asteroids (NEAs). We define a "comet-like" orbit as one having a Tisserand invariant T_J under 3 (but only including objects that are NEAs or otherwise unusual). Visible-wavelength data were also obtained, so geometric albedos (in the Cousins R band) and effective radii are presented for 25 objects (plus one more with 3 σ limits) as derived using the NEA Thermal Model. Nine of our objects were observed at two or more mid-infrared wavelengths, and in all cases the low-thermal inertia thermal model was found to be applicable, with various values of the beaming parameter. Our work more than quintuples the total number of observationally constrained albedos among $T_J < 3$ asteroids to 32. Defining the "comet-like" albedos as those below 0.075, we find that 64% ± 5% of the sample has comet-like albedos. Objects in comet-like orbits with comet-like albedos are candidates for being dormant or extinct comets. Indeed, one of our targets, 2001 OG_{108}, became active again a few months after our observations. We find a very strong correlation between the albedo distribution and T_J, with the percentage of dark $T_J < 3$ asteroids being much greater than that of the $T_J > 3$ NEAs. There are 10 NEAs among the 32 objects, and of those, 53% ± 9% have comet-like albedos. With the current crop of NEAs, this implies that about 4% of all known NEAs are extinct comets. A comparison of the histogram of $T_J < 3$ asteroid albedos with that of active cometary nuclei shows that the former has a larger spread.

Key words: comets: general — infrared: solar system — minor planets, asteroids

1. INTRODUCTION

At the end of its active life, a cometary nucleus can reach dormancy (where activity is very sporadic) and extinction (where activity no longer happens at all). As activity proceeds, the near-surface volatiles are depleted, and a rubble mantle is built up on the nucleus's surface (Rickman et al. 1990; Kührt & Keller 1994; Benkhoff & Huebner 1996; Jewitt 2002). The mantle is porous and a poor thermal conductor, eventually becoming so thick that subsurface volatiles cannot be warmed up to sublimation temperature. The usual orbital cycle of cometary activity ceases, and the nucleus is observationally identical to some asteroids. Hartmann et al. (1982, 1987) early on observed similarities in the surface properties of active comets, suspected extinct comets, and primitive asteroids. Observational evidence for cometary extinction is found in 107P/Wilson-Harrington (Bowell et al. 1992; Fernández et al. 1997), in which activity was detected at the discovery epoch in 1949 but never since.

The disparity between the dynamical timescale and the active lifetimes of the comets (Öpik 1963; Wetherill 1979; Levison & Duncan 1994, 1997; Fernández et al. 2002a) implies that there should be a significant population of dormant and extinct comets in the inner solar system, mostly from the ecliptic comet population (i.e., the Jupiter-family comets [JFCs]). In the last few years several high-inclination, high-eccentricity asteroids—referred to as "Damocloids"—have been discovered that are likely dormant or extinct members of the isotropic comet population (e.g., Jewitt 2005).

Here we address the question of how many dormant or extinct comets are masquerading as asteroids. We have focused on asteroids in comet-like orbits, some of which are near-Earth asteroids (NEAs; defined as having perihelion distance q under 1.3 AU) and some of which are "unusual" asteroids (UAs; inner solar system objects with high eccentricities and/or inclinations but with $q > 1.3$ AU). There is no definitive observational test to determine whether a given asteroid is actually a dormant or extinct comet, so we have taken a statistical approach and are determining the albedo distribution of these objects. This method is not perfect, since there are main-belt asteroids with comet-like albedos that are the source for some such objects (Gradie et al. 1989; Bottke et al. 2002; Morbidelli et al. 2002). Nonetheless, our method provides an important observational test that is independent of dynamical models. We consider an asteroid in a comet-like orbit with a comet-like albedo to be an extinct comet candidate.

In terms of the geometric albedo, p, we define "comet-like" based on the currently known distribution for cometary nuclei. Campins & Fernández (2002) and Lamy et al. (2004) reviewed the albedos and found a range of $p = 0.02$–0.06 from 13 objects (excluding the active Centaurs Chiron [Fernández et al. 2002b] and Schwassmann-Wachmann 1 [Stansberry et al. 2004]). As we explain in more detail later, we set the upper bound to the "comet-like" R-band geometric albedo p_R to be 0.075.

In terms of the orbit, our criterion uses the Tisserand invariant T_J (Tisserand 1896),

$$T_J = \frac{a_J}{a} + 2\cos i\sqrt{\frac{1-e^2}{a_J/a}}, \quad (1)$$

where a, e, and i are the semimajor axis, eccentricity, and inclination, respectively, of the object's orbit, and $a_J = 5.2$ AU is the semimajor axis of Jupiter's orbit. This quantity is a constant of motion in the restricted three-body problem and is related to an object's encounter velocity with Jupiter. Most main-belt

[1] Visiting Astronomer at W. M. Keck Observatory, which is jointly operated by the California Institute of Technology and the University of California.
[2] Current address: Department of Terrestrial Magnetism, Carnegie Institution of Washington, 5241 Broad Branch Road NW, Washington, DC 20015.

asteroids have $T_J > 3$, most JFCs have $2 < T_J < 3$, and Halley-family and long-period comets (HFCs and LPCs) have $T_J < 2$ (Levison 1996). Therefore, we declare that an asteroid has a "comet-like" orbit if $T_J < 3$, i.e., if the Tisserand value is "low." Note that in all discussion we exclude main-belt objects, Hildas, Trojans, and Cybeles that happen to have $T_J < 3$, since these objects are for the most part dynamically separate. We are only concerned here with NEAs and UAs.

As of 2004 December 4, almost 400 known UAs and about 220 known NEAs have $T_J < 3$. This is about 7% of the entire known NEA population. Conversely, of the ~260 known JFCs, only 12 (about 4.5%) have $T_J > 3$. The extreme cases are 107P/(4015) Wilson-Harrington ($T_J = 3.09$) and 133P/(7968) Elst-Pizarro ($T_J = 3.18$), which certainly have atypical activity behaviors in addition to their unusual orbits.

In this paper we describe radiometric constraints on the albedos p_R and effective radii R of 26 asteroids with $T_J < 3$. In § 2 we discuss the observations and reduction of the data, and in § 3 we describe the conversion from photometry to physical quantities p_R and R. Section 4 discusses some details of specific objects. In § 5 we discuss our findings in the context of published results on other objects with $T_J < 3$ and other NEAs. Our data bring to 32 the total number of $T_J < 3$ asteroids with observationally constrained albedos.

2. OBSERVATIONS AND REDUCTION

We observed most of our 26 targets at the Keck I telescope using the Long-Wavelength Spectrometer (LWS) camera (Jones & Puetter 1993). A few targets were observed at the Keck II telescope using JPL's Mid-Infrared Large-well Imager (MIRLIN; Ressler et al. 1994) and at the United Kingdom Infrared Telescope (UKIRT) using the Michelle camera (Glasse et al. 1997). The three cameras had pixel scales of 0.″085, 0.″138, and 0.″21 pixel^{-1}, respectively, and array sizes of 128×128, 128×128, and 320×240, respectively. Depending on observing conditions and available filters, the objects were observed at wavelengths ranging from 8.9 to 20.8 μm. The filters all had bandpass widths (to 50% of peak transmission) that were about 10% of the central wavelength. Visible-wavelength data were collected at the University of Hawaii 88 inch (2.2 m) telescope using a 2100×2068 pixel Tektronix charge-coupled device (CCD) with a pixel scale of 0.″22 pixel^{-1}. We observed the targets in an R filter that closely approximated the standard Cousins R bandpass. A list of all the observing runs in which data for this project were taken is given in Table 1. For 19 of our targets, data in the two wavelength regimes (mid-IR and visible) were collected simultaneously. For five others, the data were not simultaneous. For two others, we only have infrared data and visible-wavelength magnitudes that were extrapolated from other published sources.

The infrared data were obtained using chopping and nodding, with a throw of 4″ at Keck I, 5″ at Keck II, and 15″ at UKIRT. Guiding with a nearby star at nonsidereal tracking rates was used for each target. We only used data obtained when sky conditions were photometric. The FWHM of the seeing disk at Keck varied between about 0.″3 and 0.″4 for narrowband wavelengths near the N band and up to 0.″5 for wavelengths near the Q band. At UKIRT the seeing FWHM was 0.″7–0.″9. Flat-fielding errors were negligible in all detectors, and in any case, we observed standard stars and science targets in the same region of the arrays.

Photometric calibration was done by using a variety of standard stars. The adopted absolute flux calibration is given in Table 2. For most stars we used Engelke (1992) functions, with parameters taken from work either by Engelke (1992) himself or by Cohen et al. (1996). For the other stars we used fluxes published by Cohen et al. (1999), interpolation of magnitudes published by Tokunaga (1984), or interpolation of fluxes collected by Hoffmann & Hora (1999). We accounted for atmospheric extinction by measuring the instrumental magnitudes of the standard stars over a range of air masses and as near in time as possible to the observations of the asteroids. To maximize the signal-to-noise ratio in photometry we applied aperture corrections based on the radial profiles of the standard stars.

TABLE 1
OBSERVING RUNS

UT Date	Telescope	Instrument	Wavelengths
2000 Jun 22	Keck I	LWS	12.5 μm
2000 Jun 23	Keck I	LWS	12.5 μm
2000 Jul 2	UH 88 inch	Tek2K	R
2000 Nov 8	Keck II	MIRLIN	11.7, 12.5, 20.8 μm
2000 Nov 8	UH 88 inch	Tek2K	R
2001 Mar 12	Keck I	LWS	10.7, 17.9 μm
2001 Oct 3	Keck I	LWS	10.7, 17.9 μm
2001 Oct 3	UH 88 inch	Tek2K	R
2001 Oct 4	Keck I	LWS	10.7, 17.9 μm
2001 Oct 4	UH 88 inch	Tek2K	R
2001 Nov 2	Keck I	LWS	10.7, 17.9 μm
2001 Nov 16	UH 88 inch	Tek2K	R
2002 Mar 28	Keck I	LWS	8.9, 12.5 μm
2002 Mar 28	UH 88 inch	Tek2K	R
2002 Sep 13	UKIRT	Michelle	11.6 μm
2002 Sep 13	UH 88 inch	Tek2K	R
2004 Mar 17	UKIRT	Michelle	9.7 μm
2004 Mar 17	UH 88 inch	Tek2K	R

The visible images were obtained while tracking at nonsidereal rates that matched the proper motion of the asteroids. The seeing FWHM varied between 0.″7 and 1.″0. Flat fields were obtained by combining dithered images of the blank twilight sky. Bias frames were obtained by combining zero-exposure images. Flux calibration, air-mass corrections, and color corrections were calculated by measurements of a variety of standard stars using the magnitudes reported by Landolt (1992).

On a given night only a limited number of NEAs and UAs with $T_J < 3$ are available. The primary limitation is that an object's mid-IR flux is commonly too faint to be observed from the ground in a feasible amount of time, even with the largest telescopes. Our target list, the orbital characteristics of which are given in Table 3, reflects the haphazard nature of target availability. Fortunately, we were able to observe a large sample of objects with orbital elements that mimic those of active comets. This is shown in Figure 1, where we have plotted T_J versus D_J, the minimum orbital intersection distance (MOID) with Jupiter. Also plotted are the known active comets and other asteroids.[3] A large majority of our targets overlap the space that is spanned by the comets. It is interesting to note that among objects with $2.6 < T_J < 3.0$, asteroids have a wide range of D_J, while active comets are mostly restricted to $D_J < 1$.

The final values of the photometry are given in Table 4, along with the number of measurements that were used to obtain each value. Note that we have rereduced the mid-IR photometry of the six objects published earlier by us (Fernández et al. 2001), and the values presented here supersede those. We wanted to have all

[3] Asteroid data provided by E. L. G. Bowell and available at ftp://ftp.lowell.edu/pub/elgb/astorb.dat.gz. Comet data provided by the Minor Planet Center and available from Marsden & Williams (2003) and http://cfa-www.harvard.edu/iau/Ephemerides/Comets/index.html.

TABLE 2

ADOPTED INFRARED STANDARD STAR FLUX DENSITIES

Star	$F_{8.9}$	$F_{9.7}$	$F_{10.7}$	$F_{11.6}$	$F_{11.7}$	$F_{12.5}$	$F_{17.9}$	$F_{20.8}$	Source
β And	...	...	235.7	...	...	...	85.9	...	1
γ Aql	...	...	67.1	...	56.8	50.3	24.9	18.5	2
α Ari	...	...	69.8	...	58.7	51.6	25.4	19.2	2
α Aur	...	...	207.7	...	...	...	75.1	...	3
α Boo	...	774.8	...	...	...	472.1	...	...	1
α CMa	...	...	124.5	...	...	...	43.4	...	4
α CMi	...	...	68.0	...	56.8	49.7	24.2	17.9	4
α CrB	...	...	...	...	...	3.47	...	...	4
γ Dra	...	...	135.0	...	...	99.7	49.1	...	1
α Hya	...	141.2	...	...	...	...	...	...	1
σ Lib	...	...	...	...	...	109.0	...	...	5
α Lyr	...	...	33.9	...	...	24.9	12.3	...	4
β Peg	...	...	337.6	...	284.0	249.8	123.4	91.6	1
μ UMa	104.5[a]	94.7[a]	...	...	70.9	62.3	...	22.8	1
α Tau	...	...	...	495.2	...	...	...	...	1

NOTES.—Ellipses indicate wavelengths we did not need for that particular standard star, and F = flux density in janskys at the subscript wavelength in microns. "Source" refers to the source of the fluxes: (1) Engelke (1992) function using the parameters by Cohen et al. (1996); (2) template file from Cohen et al. (1999); (3) Engelke (1992) function using the parameters by Engelke (1992); (4) interpolation from the N and Q magnitudes by Tokunaga (1984); and (5) interpolation from fluxes reported by Hoffmann & Hora (1999).

[a] This flux accounts for the known SiO absorption band in this object's spectrum near 9 μm.

TABLE 3

ORBITAL PARAMETERS

Desig.	No.	a	e	i	Q	T_J	D_J	Type
1999 JG_{63}	...	2.964	0.556	8.0	4.61	2.998	0.867	MC
1999 LE_{31}	...	8.163	0.472	151.9	12.07	−1.311	0.538	D
2000 DG_{8}	...	10.790	0.793	129.4	19.35	−0.632	1.867	D
2000 EJ_{37}	...	4.690	0.704	10.2	7.99	2.437	0.596	MC
2000 HE_{46}	...	23.980	0.902	158.4	45.61	−1.507	0.134	D
2000 OG_{44}	(18916)	3.872	0.581	7.3	6.12	2.737	0.623	UA
2000 PG_{3}	...	2.825	0.859	20.5	5.25	2.549	0.937	Ap
2000 SB_{1}	...	3.342	0.541	22.2	5.15	2.805	0.695	UA
2000 VU_{2}	(37117)	6.945	0.554	13.7	10.79	2.618	1.280	UA
2000 YN_{30}	...	3.918	0.580	22.4	6.19	2.635	0.400	UA
2001 KX_{67}	...	3.140	0.573	20.3	4.94	2.851	1.635	MC
2001 NX_{17}	(32511)	5.058	0.427	8.9	7.22	2.790	0.646	UA
2001 OB_{74}	...	3.039	0.504	16.8	4.57	2.976	0.943	UA
C/2001 OG_{108}	...[a]	13.300	0.925	80.2	25.60	0.597	0.962	Ap, D
2001 QF_{6}	...	7.128	0.687	24.3	12.03	2.280	0.256	UA
2001 QL_{169}	...	3.100	0.508	14.4	4.68	2.966	0.795	UA
2001 QQ_{199}	...	5.322	0.436	42.3	7.64	2.323	1.937	UA
2001 RC_{12}	...	3.242	0.635	27.2	5.30	2.689	0.150	Am
2001 SJ_{262}	...	2.962	0.568	10.7	4.64	2.977	0.876	Ap
2001 TX_{16}	...	3.583	0.598	8.1	5.73	2.769	0.384	MC
2002 CX_{58}	...	2.798	0.659	2.5	4.64	2.962	0.327	Ap
2002 CX_{174}	...	3.072	0.511	21.6	4.64	2.922	0.994	MC
2002 RP_{120}	(65407)	56.130	0.956	119.1	109.79	−0.845	2.502	D
2003 UL_{12}	...	3.304	0.698	19.7	5.61	2.649	1.558	Ap
2003 WV_{157}	...	3.134	0.521	20.4	4.77	2.902	1.463	MC
2003 WN_{188}	...	14.538	0.849	26.9	26.88	1.934	1.273	D

NOTES.—"Desig." = designation, "No." = permanent asteroid number, a = semimajor axis in AU, e = eccentricity, i = inclination in degrees, Q = aphelion distance in AU, T_J = Tisserand invariant, D_J = minimum orbit intersection distance with Jupiter's orbit in AU, and "Type" = dynamical type. In that column, "Am" = Amor, "Ap" = Apollo, "MC" = Mars crosser, "D" = Damocloid, and "UA" = unusual asteroid not a member of any other group. Orbital elements courtesy of JPL's Horizons online service.

[a] This object technically no longer has the asteroid designation but only the cometary designation, which in full is C/2001 OG_{108} (LONEOS).

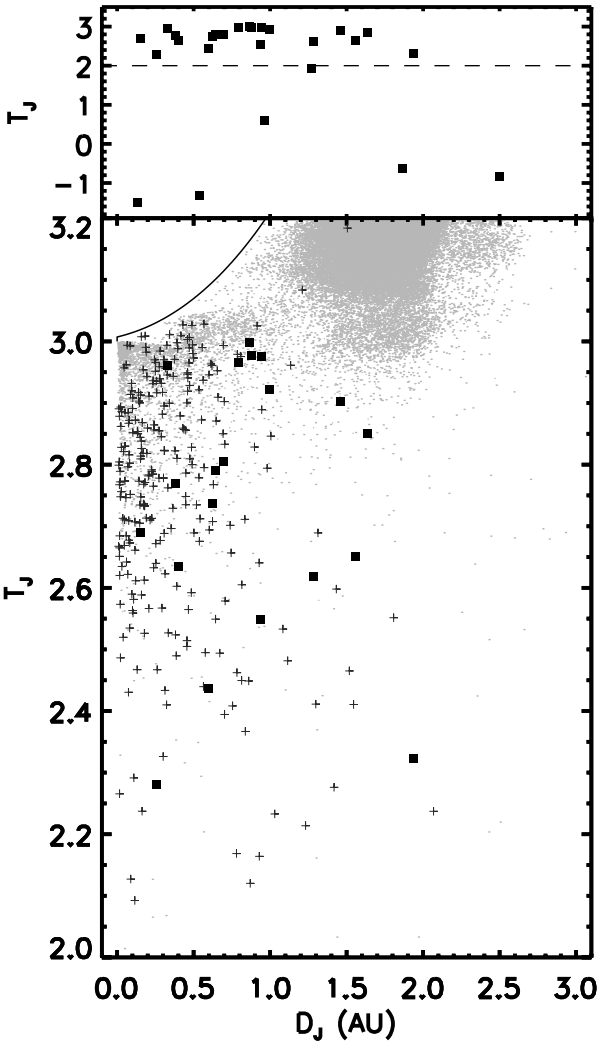

FIG. 1.—Plot of the Tisserand invariant T_J vs. the MOID D_J for selected small bodies in the solar system. Both quantities are calculated with respect to Jupiter. Members of our sample of 26 asteroids are denoted with squares, other asteroids with dots, and active JFCs with crosses. The top panel shows only our observed asteroids and excludes the other small bodies for clarity. The bottom panel is a close-up of the $T_J > 2$ region. The solid line marks the boundary of a dynamically impossible zone. Note that the large majority of our observed asteroids overlap the space spanned by the active comets, not only in T_J but in D_J as well.

our asteroid photometry linked to a set of standard star fluxes that is as accurate as possible. For this reason we have updated flux estimates for some standards.

3. ANALYSIS

The basic radiometric method to obtain an effective radius, R, and geometric albedo, p, is to solve two equations with these two unknowns, first done about 35 years ago (Allen 1970; Matson 1972; Morrison 1973) and described in detail by Lebofsky & Spencer (1989):

$$F_{\rm vis}(\lambda_{\rm vis}) = \frac{F_\odot(\lambda_{\rm vis})}{(r/1\ {\rm AU})^2} R^2 p \frac{\Phi_{\rm vis}(\alpha)}{\Delta^2}, \tag{2a}$$

$$F_{\rm mir}(\lambda_{\rm mir}) = \epsilon \int B_\nu[T(pq,\ \eta,\ \epsilon,\ \theta,\ \phi),\ \lambda_{\rm mir}] d\phi\, d\cos\theta R^2 \frac{\Phi_{\rm mir}(\alpha)}{\pi\Delta^2}, \tag{2b}$$

where F is the measured flux density of the object at wavelength λ in the visible ("vis") or mid-infrared ("mir"); $F_\odot$ is the flux density of the Sun at Earth as a function of wavelength; r and Δ are the object's heliocentric and geocentric distances, respectively; Φ is the phase darkening in each regime as a function of phase angle α; B_ν is the Planck function; ϵ is the infrared emissivity; η is a factor to account for infrared beaming; and T is the temperature. The temperature itself is a function of p, ϵ, η, surface planetographic coordinates θ and ϕ, and the (dimensionless) phase integral q, which links the geometric and Bond albedos. For simplicity, and often also for lack of detailed shape information, the modeled body is assumed to be spherical, so all radii given here are "effective" radii. Note that T generally depends on $1 - pq$, which means that for low albedos the mid-IR photometry is relatively insensitive to the albedo, so the albedo is constrained primarily by the visible photometry alone.

The surface map of temperature is calculated using a model of the thermal behavior. Unfortunately, the thermal inertias are largely unknown. To avoid this problem, two simple thermal models, covering the extremes of thermal behavior, are often employed (Lebofsky & Spencer 1989). The models are widely used, so results are easy to compare. The two models apply to slow and fast rotators. The former (also known as the "standard thermal model" [STM]) applies if the rotation is so slow (or the thermal inertia so low) that every point on the surface is in instantaneous equilibrium with the impinging solar radiation. In this case the temperature is a maximum at the subsolar point and decreases as $(\cos\vartheta)^{1/4}$, where ϑ is the local solar zenith angle. The latter (also known as the "isothermal latitude model" [ILM]) applies if the rotation is so fast (or the thermal inertia so high) that a surface element does not appreciably cool as it spins away from local noon and out of sunlight. The rotation axis is assumed to be perpendicular to the Sun-object-Earth plane. In this case the temperature only depends on the latitude of the surface element.

The other parameters to the models are ϵ, $\Phi_{\rm mir}$, $\Phi_{\rm vis}$, q, and η. Emissivity for rocks is close to unity (Morrison 1973), and we assume $\epsilon = 0.9$ here (a common assumption, although it has only a small effect anyway). For $\Phi_{\rm vis}$, we use the IAU-adopted H, G formalism (Bowell et al. 1989). The slope parameter G ranges between 0.0 and 0.4 for almost all asteroids. We adopt $G = 0.05 \pm 0.05$ in light of recent results indicating that comets and comet-related bodies have very steep phase curves (Fernández et al. 2000; Schaefer & Rabinowitz 2002; Sheppard & Jewitt 2002; Bauer et al. 2003; Jewitt & Sheppard 2004). The value of G determines q, but since that has a minor effect on the modeling, we adopt $q = 0.3$ (cf. Buratti et al. 2004), which is the integral's value for $G = 0.05$.

The choices of $\Phi_{\rm mir}$ and η are often the most important determinants in deriving an accurate R and p. We have used the NEA Thermal Model (NEATM) devised by Harris (1998) to determine what to use for these quantities. This model's characterization of $\Phi_{\rm mir}$ and η is the primary distinguishing difference from the pure STM. For $\Phi_{\rm mir}$, Harris (1998) argued that a more sophisticated phase law is needed than the usual linear phase coefficient. His approach is to calculate a phase effect based simply on the surface integral of the thermal flux over the Earth-facing hemisphere. In our modeling, we employed this method and calculated the surface integral.

As for η, the standard value of 0.756 (Lebofsky et al. 1986) was originally derived for Ceres. However, recent work (Harris 1998; Harris et al. 1998; Harris & Davies 1999; Delbó et al. 2003) indicates that small asteroids can have a variety of values for η. Thus, we have made the beaming parameter a variable to be

TABLE 4

Log of Observations

Desig.	UT Date	UT	r	Δ	α	λ	F_λ	n
1999 JG_{63}	2004 Mar 17	13:09–13:40	2.409	1.483	11.0	R	17.296 ± 0.032[a]	5
1999 JG_{63}	2004 Mar 17	12:40–13:43	2.409	1.483	11.0	9.7	25 ± 5	1
1999 LE_{31}	2000 Jul 2	07:32	5.267	5.311	11.0	R	20.440 ± 0.050	1
1999 LE_{31}	2000 Jun 22	07:11–07:27	5.238	5.118	11.2	12.5	6.5 ± 1.4[b]	4
1999 LE_{31}	2000 Jun 23	06:32–06:49	5.240	5.137	11.2	12.5	4.9 ± 0.6[b]	2
2000 DG_8	2000 Nov 8	12:01–12:50	2.319	1.728	22.9	R	16.826 ± 0.016	8
2000 DG_8	2000 Nov 8	12:35–13:35	2.319	1.728	22.9	11.7	385 ± 30[b]	4
2000 DG_8	2000 Nov 8	...	2.319	1.728	22.9	12.5	399 ± 36[b]	13
2000 DG_8	2000 Nov 8	...	2.319	1.728	22.9	20.8	640 ± 103[b]	3
2000 EJ_{37}	2001 Oct 3	14:27–15:16	3.108	2.354	14.0	R	18.370 ± 0.020	4
2000 EJ_{37}	2001 Oct 3	14:19–14:47	3.108	2.354	14.0	10.7	32.9 ± 9.7	2
2000 HE_{46}	2000 Jul 2	06:16	2.562	2.689	22.2	R	20.110 ± 0.020	1
2000 HE_{46}	2000 Jun 23	08:01–08:20	2.526	2.470	23.5	12.5	27.0 ± 2.1[b]	5
2000 OG_{44}	2000 Nov 8	06:07–06:19	1.665	0.920	30.6	R	16.390 ± 0.010	2
2000 OG_{44}	2000 Nov 8	06:07–06:22	1.665	0.920	30.6	12.5	647 ± 32[c]	3
2000 OG_{44}	2000 Nov 8	...	1.665	0.920	30.6	20.8	619 ± 40[c]	4
2000 PG_3	2000 Nov 8	05:11–05:35	1.064	0.929	59.1	R	17.857 ± 0.013	2
2000 PG_3	2000 Nov 8	04:37–05:20	1.064	0.929	59.1	12.5	338 ± 58[c]	9
2000 PG_3	2000 Nov 8	...	1.064	0.929	59.1	20.8	493 ± 67[b]	2
2000 SB_1	2000 Nov 8	11:15–11:28	1.554	0.673	25.6	R	16.270 ± 0.010	2
2000 SB_1	2000 Nov 8	10:58–11:48	1.554	0.673	25.6	11.7	1060 ± 27[c]	2
2000 SB_1	2000 Nov 8	...	1.554	0.673	25.6	12.5	1085 ± 53[b]	8
2000 SB_1	2000 Nov 8	...	1.554	0.673	25.6	20.8	1200 ± 300[b]	3
2000 VU_2	2001 Mar 12	06:34–07:02	3.142	3.233	17.9	10.7	22.6 ± 2.1	1
2000 VU_2	2001 Mar 12	...	3.142	3.233	17.9	17.9	58.2 ± 5.9	1
2000 YN_{30}	2001 Mar 12	07:35–07:50	1.651	1.291	37.0	10.7	12.5 ± 1.7	1
2001 KX_{67}	2001 Oct 3	11:44–12:25	1.349	0.489	36.7	R	17.005 ± 0.027	4
2001 KX_{67}	2001 Oct 3	11:55–12:52	1.349	0.489	36.7	10.7	541 ± 71	1
2001 KX_{67}	2001 Oct 3	...	1.349	0.489	36.7	17.9	603 ± 58[d]	1
2001 NX_{17}	2001 Nov 16	04:36–05:28	3.218	3.441	16.6	R	18.939 ± 0.021	3
2001 NX_{17}	2001 Nov 2	05:58–06:58	3.181	3.220	17.8	10.7	38.8 ± 2.0	2
2001 OB_{74}	2001 Oct 4	08:54–10:34	1.818	0.943	21.3	R	19.261 ± 0.040	3
2001 OB_{74}	2001 Oct 4	09:52–10:20	1.818	0.943	21.3	10.7	29.5 ± 2.9	2
2001 OG_{108}	2001 Oct 4	...	2.530	1.561	7.0	R	16.300 ± 0.009	6
2001 OG_{108}	2001 Oct 4	...	2.530	1.561	7.0	10.7	421 ± 20	2
2001 OG_{108}	2001 Oct 4	...	2.530	1.561	7.0	17.9	742 ± 34	2
2001 QF_6	2001 Oct 3	08:26–09:20	2.497	1.723	17.6	R	19.435 ± 0.028	7
2001 QF_6	2001 Oct 3	08:21–08:40	2.497	1.723	17.6	10.7	29.2 ± 3.1	1
2001 QL_{169}	2001 Oct 4	12:23–13:00	1.700	0.773	18.9	R	20.190 ± 0.050	5
2001 QL_{169}	2001 Oct 4	12:58–13:20	1.700	0.773	18.9	10.7	6.7 ± 2.8	1
2001 QQ_{199}	2001 Nov 16	05:56–06:28	3.039	2.169	10.5	R	17.126 ± 0.015	3
2001 QQ_{199}	2001 Nov 2	09:12–10:27	3.054	2.097	5.9	10.7	174.6 ± 10.1	1
2001 QQ_{199}	2001 Nov 2	...	3.054	2.097	5.9	17.9	392 ± 20	2
2001 RC_{12}	2001 Oct 4	14:37–15:20	1.197	0.697	56.6	R	17.444 ± 0.015	4
2001 RC_{12}	2001 Oct 4	14:52–14:54	1.197	0.697	56.6	10.7	241 ± 13	1
2001 SJ_{262}	2001 Oct 3	12:43–14:01	1.280	0.289	12.9	R	18.243 ± 0.020	10
2001 SJ_{262}	2001 Oct 3	13:17–14:14	1.280	0.289	12.9	10.7	20.3 ± 2.4	2
2001 TX_{16}	2001 Nov 16	12:21–12:50	1.592	0.835	32.0	R	15.857 ± 0.017[e]	3
2001 TX_{16}	2001 Nov 2	14:13–15:15	1.660	0.985	33.0	10.7	119.6 ± 8.8	1
2001 TX_{16}	2001 Nov 2	...	1.660	0.985	33.0	10.7	135.7 ± 8.8[e]	1
2001 TX_{16}	2001 Nov 2	14:13–15:15	1.660	0.985	33.0	17.9	336 ± 69	1
2001 TX_{16}	2001 Nov 2	...	1.660	0.985	33.0	17.9	242 ± 30[e]	1
2002 CX_{58}	2002 Mar 28	14:47–15:25	0.959	0.132	103.5	R	21.570 ± 0.120	4
2002 CX_{58}	2002 Mar 28	15:02–15:20	0.959	0.132	103.5	12.5	6.1 ± 2.0	2
2002 CX_{174}	2002 Mar 28	11:26–11:55	1.593	0.602	7.2	R	17.155 ± 0.016	8
2002 CX_{174}	2002 Mar 28	11:40–11:55	1.593	0.602	7.2	8.9	136 ± 5	1
2002 CX_{174}	2002 Mar 28	...	1.593	0.602	7.2	12.5	254 ± 8	1
2002 RP_{120}	2002 Sep 13	14:13–14:30	2.486	2.063	23.3	R	16.882 ± 0.030	3
2002 RP_{120}	2002 Sep 13	13:57–14:12	2.486	2.063	23.3	11.6	170 ± 8	4
2003 UL_{12}	2004 Mar 17	14:04–14:10	1.624	0.735	23.6	R	18.417 ± 0.043	3

TABLE 4—*Continued*

Desig.	UT Date	UT	r	Δ	α	λ	F_λ	n
2003 UL_{12}	2004 Mar 17	13:53–14:50	1.624	0.735	23.6	9.7	<25[f]	1
2003 WV_{157}	2004 Mar 17	08:29–08:55	1.539	0.744	32.4	R	17.838 ± 0.110	5
2003 WV_{157}	2004 Mar 17	08:01–08:22	1.539	0.744	32.4	9.7	160 ± 20	1
2003 WN_{188}	2004 Mar 17	09:32–09:55	2.212	1.412	19.2	R	17.223 ± 0.028	5
2003 WN_{188}	2004 Mar 17	09:46–09:56	2.212	1.412	19.2	9.7	160 ± 10	1

NOTES.—"Desig." = designation, r = heliocentric distance in AU, Δ = geocentric distance in AU, α = phase angle in degrees, λ = wavelength or band of observation, F_λ = flux density in magnitudes for visible wavelengths and millijanskys for infrared wavelengths, and n = number of measurements used.

[a] A light-curve effect of 0.09 mag was noted in the R-band photometry.

[b] Flux is $\leq 1\ \sigma$ away from that published by us earlier (Fernández et al. 2001).

[c] Flux is $\geq 1\ \sigma$ away from that published by us earlier (Fernández et al. 2001). For 2000 OG_{44}, this is due to a large downward revision in the adopted flux for calibrator β Peg. For 2000 PG_3, this is due to an error we found in the original reduction. For 2000 SB_1, the flux is within 2 σ of the old value.

[d] The R-band magnitude changed by +0.1 mag between the times that the two infrared wavelengths were observed. Hence, this 17.9 μm flux density was multiplied by 1.1 before modeling.

[e] A significant light-curve effect was noted at all three wavelengths. See § 4 for details.

[f] This is a 3 σ upper limit.

fit, and our modeling routines return values for three physical parameters, R, p_R, and η.

Note, however, that a rigorous χ^2 analysis with three parameters requires four data points. Unfortunately, we have the necessary number of measurements (photometry at three mid-IR wavelengths plus one visible wavelength) for only two of our targets. For seven targets, we have three data points, and for 17 targets, we have only two data points. To overcome this, we proceed to "fit" the photometry as follows. For each of the seven targets with three points, we find the ranges of η, R, and p such that a model spectral energy distribution would pass within 1 σ of all data points. For each of the 17 targets with two points, we assume two extreme values of η, 0.7 and 1.3, and derive the ranges of R and p such that a model spectral energy distribution would pass within 1 σ of both data points. While this method cannot yield a rigorous "fit" and Gaussian error estimates, it

TABLE 5

EFFECTIVE RADII AND GEOMETRIC ALBEDOS

Object	No.	N	S?	R (km)	p_R	η
1999 JG_{63}	...	2	Y	2.4 ± 0.5	0.193 ± 0.077	(0.7–1.3)
1999 LE_{31}	...	2	N	8.4 ± 2.1[a]	0.056 ± 0.026[a]	(0.7–1.3)
2000 DG_8	...	4	Y	7.8 ± 1.3	0.053 ± 0.017	0.95 ± 0.25
2000 EJ_{37}	...	2	Y	5.4 ± 1.2	0.069 ± 0.030	(0.7–1.3)
2000 HE_{46}	...	2	N	3.2 ± 0.6	0.045 ± 0.016	(0.7–1.3)
2000 OG_{44}	(18916)	3	Y	2.8 ± 0.3	0.111 ± 0.024	0.4–0.6
2000 PG_3	...	2	Y	2.1 ± 0.3	0.046 ± 0.012	(0.7–1.3)
2000 SB_1	...	4	Y	2.8 ± 0.6	0.056 ± 0.024	0.75 ± 0.35
2000 VU_2	(37117)	3	N	5.6 ± 0.8	0.088 ± 0.044	0.57–1.15
2000 YN_{30}	...	2	N	0.85 ± 0.15	0.096 ± 0.032	(0.7–1.3)
2001 KX_{67}	...	3	Y	1.6 ± 0.3	0.045 ± 0.015	0.5–1.5
2001 NX_{17}	(32511)	2	N	8.4 ± 2.0	0.043 ± 0.019	(0.7–1.3)
2001 OB_{74}	...	2	Y	1.0 ± 0.2	0.061 ± 0.021	(0.7–1.3)
C/2001 OG_{108}	...	3	Y	6.8 ± 0.5	0.054 ± 0.008	0.52–0.75
2001 QF_6	...	2	Y	2.7 ± 0.5	0.040 ± 0.016	(0.7–1.3)
2001 QL_{169}	...	2	Y	0.36 ± 0.05	0.107 ± 0.033	(0.7–1.3)
2001 QQ_{199}	...	3	N	8.2 ± 0.6	0.059 ± 0.009	0.56–0.84
2001 RC_{12}	...	2	Y	1.6 ± 0.2	0.080 ± 0.023	(0.7–1.3)
2001 SJ_{262}	...	2	Y	0.17 ± 0.03	0.177 ± 0.051	(0.7–1.3)
2001 TX_{16}	...	3	N[b]	2.8 ± 1.0	0.181 ± 0.114	0.53–2.96
2002 CX_{58}	...	2	Y	0.065 ± 0.009	0.126 ± 0.035	(0.7–1.3)
2002 CX_{174}	...	3	Y	1.5 ± 0.1	0.031 ± 0.005	0.96–1.34
2002 RP_{120}	(65407)	2	Y	7.3 ± 1.4	0.098 ± 0.036	(0.7–1.3)
2003 UL_{12}	...	2	Y	<0.82[c]	>0.093[c]	(1.3)
2003 WV_{157}	...	2	Y	1.8 ± 0.3	0.050 ± 0.018	(0.7–1.3)
2003 WN_{188}	...	2	Y	5.0 ± 1.1	0.050 ± 0.021	(0.7–1.3)

NOTES.—"N" gives the number of wavelengths used in the analysis and is equal to the number of mid-IR wavelengths plus one (the one visible wavelength), "S?" indicates whether the mid-IR and visible data were obtained simultaneously, R is the effective radius in kilometers, p_R is the R-band geometric albedo, and η is the beaming parameter, with parentheses indicating assumed values.

[a] Radius and albedo are derived from the average of mid-IR fluxes measured on two nights.

[b] Published light curves of this object let us derive the rotational context of our nonsimultaneous observations.

[c] Radius and albedo are 3 σ upper and lower limits, respectively. Lower values of η result in lower radii and higher albedos.

does provide some measure of the systematic uncertainty in the physical quantities.

With the photometry from Table 4 and the thermal model described here, we derive and list in Table 5 the resulting values for R, p_R, and η. Table 5 also lists the number of data points ("N") that were used for the fit. Note that our modeling scheme has changed since we published observations of the six original objects (Fernández et al. 2001). The primary difference is that we now use NEATM's style for estimating infrared phase darkening, and we use the slope parameter G (Bowell et al. 1989) for estimating visible phase darkening. We believe this provides a more realistic estimate of phase effects than the linear phase laws used in our older work. Since we observed many targets at moderate or high phase angle, this can have a significant effect on the final radius and albedo.

4. NOTES ON SPECIFIC OBJECTS

Of our 26 targets, 19 were observed simultaneously in both wavelength regimes ("Y" in the "S?" column in Table 5). Of the remaining seven, in all cases but one (mentioned below), extensive light-curve data that would have let us remove the rotational effects unfortunately did not exist. However, in each case we did correct the visible magnitude for the different observing geometries (r, Δ, and α) of the two epochs, and the results in Table 5 reflect this.

2000 OG_{44}.—In our earlier work we had assumed that $0.75 \leq \eta \leq 1.25$, whereas our current modeling lets η vary as another parameter to be fit. We find that $0.4 \leq \eta \leq 0.6$ better satisfies this object's photometry. Qualitatively, a lower beaming parameter implies that there is more beaming and that the surface is probably rougher. (Conversely, a higher η implies less beaming and more thermal inertia, placing more of the thermal emission on the object's dark side.) More beaming and roughness imply that the surface temperature is higher. Thus, for a given measured mid-IR flux, one needs a smaller radius to explain it, which propagates to needing a larger albedo to explain the visible photometry. Thus, 2000 OG_{44}'s geometric albedo is larger than what we derived in our earlier work.

2000 PG_3.—The fluxes are incompatible with NEATM for reasonable values of the beaming parameter and geometric albedo. A rapid-rotator model nominally fits the data better, but we believe this is an unlikely explanation; Delbó et al. (2003) observed this object at five mid-IR wavelengths and, while they were also unable to constrain η, their photometry is much closer to that of a NEATM than a rapid-rotator model. Since our visible-wavelength photometry does not fully overlap in time our mid-IR observations, it is possible that the mid-IR data show a light-curve effect.

The radius and albedo reported in Table 5 are based on the 12.5 μm photometry alone, since this data point is less prone to systematic problems. In comparison, Delbó et al. (2003) derived a radius of 2.3 ± 0.3 km and a geometric albedo of 0.042 ± 0.013, in agreement with our results. An analysis of our data based on the 20.8 μm photometry alone would yield a radius of 2.7 ± 0.2 km and an albedo of 0.028 ± 0.005.

2000 VU_2 and 2000 YN_{30}.—No visible wavelength data at all were obtained for these objects. Therefore, we assumed that the known V-band absolute magnitudes $H = 13.2$ and 17.2, respectively, were valid, and from these numbers estimated potential R-band magnitudes. We assumed a $V - R$ color of 0.4 and assigned a generous error estimate of ± 0.5 mag to each magnitude.

2001 OG_{108}.—Abell et al. (2005) present extensive data and analyses of this object, which was briefly active (and so received a cometary designation) for only a few months around perihelion in early 2002. They discuss the nucleus's radius, shape, albedo, rotation period, and spectral reflectance, including asteroid and meteorite affinities. All data (including ours) were obtained before cometary activity initiated. The same data presented here are presented by those workers. The albedo that they report is lower than that listed in Table 5, owing to the use of $\eta \approx 1$ in earlier modeling. As shown in Table 5, our latest modeling indicates that smaller beaming parameters better satisfy the photometry.

2001 TX_{16}.—Our mid-IR and visible photometry of this object were not taken simultaneously, but we can derive a robust radius and albedo using other reports of this object's light curve. P. Pravec (2004, private communication) has found that a rotation period of 4.80070 ± 0.00004 hr satisfies light-curve observations by Yang et al. (2003) and F. Hroch (2004, private communication)[4] that took place within a few months of our observations. The peak-to-valley range of the light curve is 0.5 mag.

Our observations were taken on UT 2001 November 2 and 16, with the two start times of the nights' data being 334.15 hr apart. This corresponds to 69.6044 ± 0.0006 rotations. On November 16 we saw 0.41 mag of brightening just in the half-hour of observations, which strongly limits the possible rotation phases for our visible data, since only at certain points in the rotation would we see a change that is almost the full range of the light curve.

Using the phased light curve presented by Yang et al. (2003) as a reference, we find that the best solution is for our visible data on November 16 to have been taken over phase 0.2–0.3, which places our infrared data on November 2 at phase 0.6–0.8. We have incorporated this rotational context into our modeling, and the radius and albedo in Table 5 reflect this.

While typical values of η satisfy the photometry, we also found that beaming parameters as high as 3 were adequate as well. This was the only object for which we found that a very high beaming parameter was possible.

2002 CX_{58}.—This object was observed at a very high phase angle. Delbó et al. (2003) suggest that the apparent best-fitting value of η increases with α. Thus, perhaps our assumed range is not applicable. Assuming instead that $1.5 < \eta < 2.1$ yields an effective radius of 0.083 ± 0.007 km and a geometric albedo of 0.078 ± 0.014. Note also that a high η would be consistent with the idea of subkilometer asteroids with very fast rotation periods (Whiteley et al. 2002) having high thermal inertia.

2003 UL_{12}.—This was the only target in the sample that we did not detect in mid-IR wavelengths. We used the 3 σ upper limit to the 11.7 μm flux to calculate an upper limit to the effective radius and a lower limit to the geometric albedo. Since albedo decreases as beaming parameter increases, we have chosen the upper bound on our adopted range for η to find the lowest possible lower limit to p_R.

5. DISCUSSION

5.1. *Albedo Distribution*

Figure 2 shows the histogram of albedos from Table 5. It includes the six other published albedos of asteroids with $T_J < 3$. These six are (3360) 1981 VA with $p = 0.10 \pm 0.03$ (Veeder et al. 1989), (3552) Don Quixote with $p = 0.020 \pm 0.006$ (Veeder et al. 1989), (20461) Dioretsa with $p = 0.03 \pm 0.01$ (Harris et al. 2001), (20898) Fountainhills with $p = 0.051 \pm 0.003$ (Tedesco et al. 2002), 1983 VA with $p = 0.067 \pm 0.006$ (Tedesco 1992), and (53319) 1999 JM_8 with $p = 0.020 \pm 0.006$, as derived from the known radar diameter and known absolute magnitude (Benner et al. 2002b).

[4] See http://www.physics.muni.cz/~hroch/tx16.html and http://sunkl.asu.cas.cz/~ppravec/newres.htm.

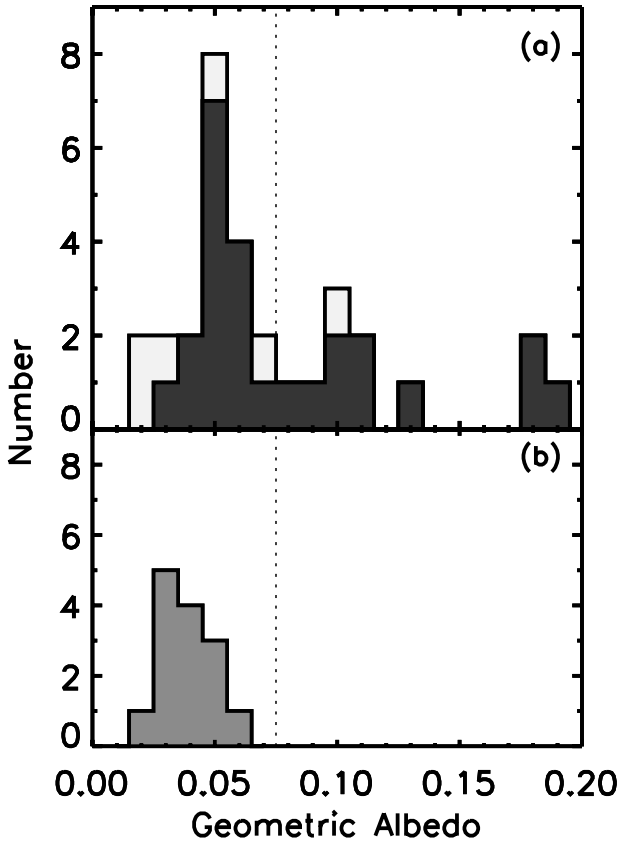

FIG. 2.—(*a*) Histogram of albedos of asteroids with $T_J < 3$. Our sample of objects (excluding the one lower limit measurement) is shown by the dark-shaded histogram, and the six other objects from the literature are added. A large fraction have low albedos; the "comet-like" albedo zone is to the left of the vertical dashed line. (*b*) Histogram of the albedo distribution of the 14 active cometary nuclei, taken from the list of Lamy et al. (2004) and with 81P/Wild 2 added in (Brownlee et al. 2004). Clearly, the spread of asteroid albedos is larger, although there are objects as dark as the active nuclei.

With our 25 albedos (excluding the lower limit of 2003 UL_{12}), there are now 31 albedos known among the $T_J < 3$ population. This sample is by no means unbiased, since it includes several objects that are of particular focused interest. However, the pseudo-random scheduling of our observing runs did force us to observe more "typical" members of the $T_J < 3$ population.

Figure 2 shows a wide range of albedos among the population, with a mode near 0.05. We can estimate the fraction of objects with comet-like albedos by setting an upper bound to a cometary albedo. The current distribution of known cometary albedos is shown in the bottom panel of Figure 2, taken from the review by Lamy et al. (2004) and with 81P/Wild 2 added in (Brownlee et al. 2004). Note that the mean cometary albedo is 0.033 ± 0.006, slightly darker than the mode of the $T_J < 3$ asteroids.

We have placed our upper bound of "comet-like" at 0.075, reasoning as follows. The known range is 0.02–0.06, but the error in an albedo measurement is frequently understated; a more realistic error bar of roughly 30% has been suggested (Delbó et al. 2003), given systematic uncertainties inherent in simple thermal modeling. Thus, to account for the large error bar and any future expansion of the range beyond the limited sample, we believe it is prudent to set an upper bound above 0.06.

Note that the measurements of cometary albedos have been reported variously in the *V* band and *R* band. Comets have red colors, so *R*-band albedos should be generally higher than *V*-band albedos. In principle, this should be accounted for in our analysis, but a ~30% uncertainty makes any difference between *V*- and *R*-band albedos statistically insignificant. For our purposes here we cap a cometary albedo in the *R*-band p_R at 0.075.

With the 32 albedos in hand, it is a simple matter to estimate the number *n* and the fraction *f* of objects in comet-like orbits that have comet-like albedos. To propagate the errors on the individual albedos into the calculation of *n* and *f*, we use a Monte Carlo technique. We find $n = 20.4 \pm 1.7$ objects, translating to $f = 63.8\% \pm 5.3\%$. Our lower limit object, 2003 UL_{12}, is above the threshold. This number changes little if we arbitrarily apply a blanket 30% error bar to all objects.

5.2. *Trends*

A plot comparing the albedos of asteroids with their Tisserand values is shown in Figure 3. All 26 of our $T_J < 3$ objects are plotted, as are the six from the literature. On the $T_J > 3$ side, 57 objects are plotted, 56 of which are NEAs (the other is a UA).

The figure dramatically demonstrates the dichotomy of asteroid albedos as a function of dynamical class. Whereas about 64% of low-Tisserand objects have comet-like albedos (as calculated in the previous subsection), that property is shared by only about 10% of the high-Tisserand NEAs. While it is likely that there are many dark high-Tisserand NEAs whose albedos await measurement, it seems unlikely that the discovery bias for high-Tisserand objects is so severe that a true bright-to-dark ratio of 1 : 2 (i.e., equivalent to the low-Tisserand ratio) could be measured as 9:1.

All objects with $T_J < 2.6$ seem to have comet-like albedos (within the error bars). Given the population statistics shown in Figure 1, probably many of these objects are dormant or extinct comets. Objects in the transition region $2.6 \leq T_J \leq 3.1$ show the largest spread in albedos, suggesting that this dynamical region is populated by a variety of sources. We conclude from Figure 3 that the asteroid albedo distribution is strongly correlated with the dynamics.

We find no other clear trends of the albedos with other orbital elements and parameters. The albedos and radii of all 32 $T_J < 3$ objects are plotted in Figure 4. There is some indication of a trend of higher albedos with smaller radii, but the correlation is not formally significant. In any case, observational limitations affect the discovery of dark versus bright small objects.

5.3. *NEAs*

In our sample of 26 objects, six are NEAs (one of which is also a Damocloid). Among the six other objects from the literature, four are NEAs (1981 VA, 1983 VA, 1999 JM_8, and Don Quixote), giving 10 NEAs in total. If we perform the same procedure on this subsample as we did in § 5.1, we find that $55\% \pm 8\%$ of the 10 NEAs have comet-like albedos. If we apply a standard 30% error bar to all albedos, the percentage becomes $53\% \pm 9\%$, which we consider to be a better estimate.

As we stated in § 1, about 7% of all known NEAs are in comet-like orbits. Multiplying the two percentages together, we find that about 4% of all known NEAs have both comet-like orbits and albedos. This represents an estimate of the fraction of dormant or extinct comets in the known NEA population.

Four important effects can affect this estimate, however. First, since two of the approximately 40 known near-Earth JFCs are actually *not* in "comet-like" orbits, we know that there may be some dormant objects on the other side of the Tisserand threshold. Second, we do not yet have a good estimate of the near-Earth HFC-LPC population or of the Damocloid population. Among the 10 NEAs in the entire $T_J < 3$ sample, one (2001 OG_{108}) is a

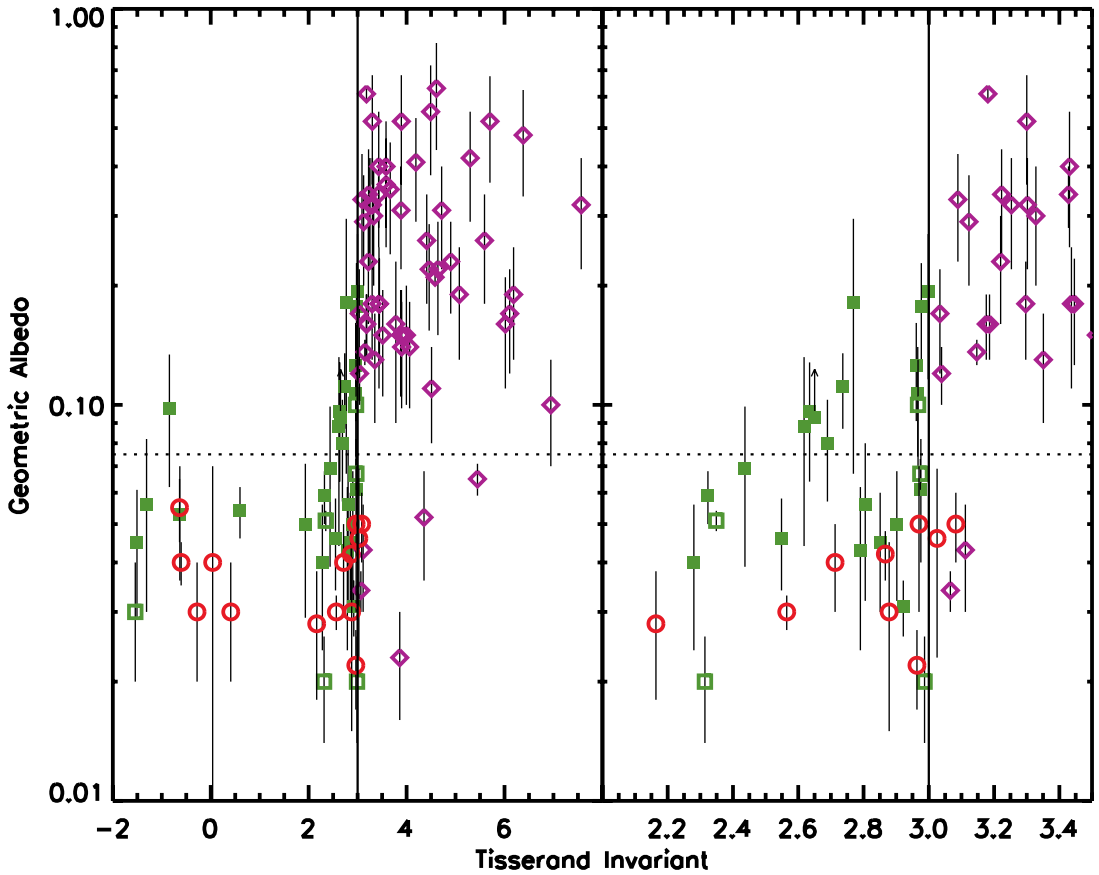

FIG. 3.—Plot of Tisserand invariant vs. known geometric albedos for $T_J < 3$ asteroids (*green squares*) and $T_J > 3$ asteroids (*purple diamonds*). Main-belt asteroids, Trojans, Cybeles, Hildas, Centaurs, and trans-Neptunian asteroids have been excluded; the plot shows only NEAs and UAs. Active cometary nuclei are represented by red circles. The 26 objects in our sample are represented by filled green squares; the six objects taken from the literature are represented by open green squares. The vertical line marks the dynamical boundary $T_J = 3$. There are 57 high-Tisserand albedos plotted, 56 of which are NEAs. The left panel shows the entire range of Tisserand values, and the right panel shows just the region near $T_J = 3$. The fraction of objects with comet-like albedos differs greatly from one side of the dynamical boundary to the other. A large fraction of the $T_J < 3$ objects have comet-like albedos. The $T_J > 3$ asteroid albedos come from the following sources: Morrison et al. (1976), Cruikshank & Jones (1977), Lebofsky et al. (1978, 1979), Green et al. (1985), Tedesco & Gradie (1987), Bell et al. (1988), Veeder et al. (1989), Tedesco (1992), Hudson & Ostro (1995), Mottola et al. (1997), Pravec et al. (1997), Harris (1998), Harris et al. (1998, 2001), Harris & Davies (1999), Tedesco et al. (2002), Benner et al. (2002a, 2002b), Delbó et al. (2003), Sekiguchi et al. (2003), and Müller et al. (2004). There are 14 cometary albedos plotted, taken from the list of Lamy et al. (2004) with 81P/Wild 2 added by Brownlee et al. (2004).

Damocloid, and indeed this object has since reactivated. Third, the estimate assumes that the NEA discovery rate reflects the true distribution of high- and low-albedo objects. It is likely that the average albedo of the known NEAs is higher than the true value of the entire population (Morbidelli et al. 2002). Fourth, not all NEAs with comet-like orbits and albedos need necessarily be former comets, since mechanisms have been identified to transport low-albedo main-belt objects into near-Earth space (Bottke et al. 2002; Morbidelli et al. 2002). The fraction of dormant and extinct comets among the NEAs could shift higher or lower depending on which of these effects dominates the current bias. Nonetheless, it is interesting to note that Bottke et al. (2002) estimate through dynamical studies that $6\% \pm 4\%$ of NEAs are dormant or extinct comets, in agreement with our observational findings.

The results of Bottke et al. (2002) and Morbidelli et al. (2002) also give insight into the relative fraction of low- (vs. high-) albedo NEAs; specifically, their model can predict that fraction for the NEAs with $T_J < 3$. For each grid point in (a, e, i) space that yields an NEA, Bottke et al. (2002) have assigned a probability of that object coming from five possible source regions, as well as the relative population of NEAs at the grid point itself. From that compilation it is straightforward to derive the statistically expected source regions of all NEAs with $T_J < 3$. The result is that they predict that 30% come from JFCs, 38% from the 3:1 mean-motion resonance with Jupiter, 24% from the outer main belt, 6% from the ν_6 resonance, and 1% from the intermediate Mars crossers. Since this model did not account for cometary nongravitational forces, the cometary contribution has uncertainty, but it seems likely that three source regions are primarily responsible for providing NEAs with $T_J < 3$.

Morbidelli et al. (2002) assigned albedo distributions to these source regions in their Table 3; they defined a "low" albedo as anything below 0.089. The fraction of low-albedo $T_J < 3$ NEAs is then just the product of a source region's contribution to the population times the fraction of low-albedo objects in the source region, summed over all five source regions. The answer is that the model predicts that 46% of $T_J < 3$ NEAs should have low albedos.

Above we derived that about 53% of the 10 NEAs in the $T_J < 3$ sample had low albedos, but this was with a more restrictive definition of "low." Furthermore, this includes object 2001 OG_{108}, which has a semimajor axis outside the scope of the model. If we match the Morbidelli et al. (2002) definition and exclude 2001 OG_{108} we find that $56\% \pm 10\%$ of the nine NEAs have low albedos. This is consistent with the prediction of Bottke

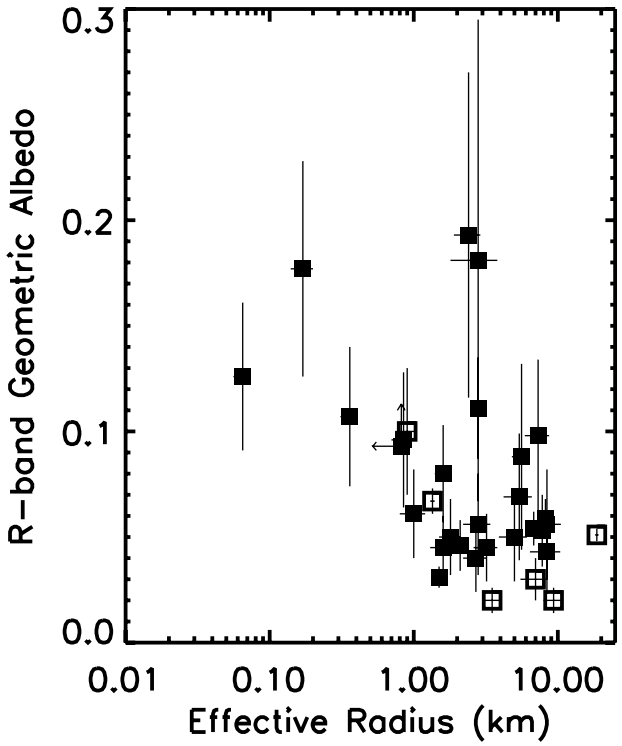

FIG. 4.—Scatter diagram of albedos and radii from our sample of 26 objects (*filled squares*) plus the sample of six objects from the literature (*open squares*). The subkilometer objects have a higher albedo, on average, than the other objects, although this may be due to discovery bias. There is no significant trend among the asteroids larger than 1 km.

et al. (2002) and Morbidelli et al. (2002). However, it is clear that a more extensive survey of NEA albedos is needed to place a more robust observational constraint on this fraction.

As a final exercise, we can use the dynamical model of Bottke et al. (2002) to determine the predicted source region for the nine NEAs in the entire $T_J < 3$ sample (excluding 2001 OG_{108}). Two objects (Don Quixote and 2000 PG_3) would have an over 90% chance of coming from the JFCs, but the remaining seven objects would have between a 0% and a 37% chance and would be more likely to come from another source region. However, it is important to note that nongravitational forces play an important role in determining what orbit a comet is in once it becomes dormant or extinct. This is epitomized by the existence of comets 2P/Encke, 107P/Wilson-Harrington, and possibly 133P/Elst-Pizarro as well. Bottke et al. (2002) would predict that 2P and 107P have a 0% and 4% chance, respectively, of coming from the JFC population. There are several other active JFCs for which Bottke et al. (2002) would predict that an asteroid in the same part of (a, e, i) space would have a roughly comparable chance of coming from either the outer main belt or the JFC population. While the Bottke et al. (2002) model provides testable predictions, effects of nongravitational forces leave murky the question of the dormant and extinct comet fraction within the NEAs. Nongravitational forces are a necessary component to understand cometary dynamics (Harris & Bailey 1998; Fernández et al. 2002a).

6. SUMMARY

We have performed a mid-IR survey of 26 near-Earth and unusual asteroids (NEAs and UAs) in comet-like orbits. Such an asteroid is one whose orbit has $T_J < 3$ (and that is not a member of the main belt, Hildas, Cybeles, or Trojans). We calculated effective radii and R-band geometric albedos for all targets (one of which has 3 σ limits). This has increased the known sample size to 32. We have reached the following conclusions:

1. We find that $64\% \pm 5\%$ of the 32 objects have comet-like albedos. A "comet-like" albedo is one with a value in the Cousins R band under 0.075. Asteroids in comet-like orbits with comet-like albedos are considered dormant or extinct comet candidates. Indeed, one of our candidates, 2001 OG_{108}, reactivated a few months after our observations.

2. There is a very strong trend of albedo with Tisserand parameter. Nearly all objects in the sample with $T_J < 2.6$ have comet-like albedos. The largest spread in albedos occurs near the dynamical threshold $T_J = 3$. Of the almost five dozen known albedos among NEAs with $T_J > 3$, only 10% are comet-like.

3. Of the 26 objects in our sample, six are NEAs, bringing the number of known albedos among NEAs with $T_J < 3$ to 10. Of those 10, $53\% \pm 9\%$ have comet-like albedos. Since 7% of all discovered NEAs have $T_J < 3$, we calculate that 4% of all known NEAs are extinct comets. This is consistent with the prediction of Bottke et al. (2002) and Morbidelli et al. (2002). However, nongravitational forces likely must be accounted for in dynamical calculations (Fernández et al. 2002a). A more thorough observational approach, one that improves on the limited sample we have presented here by studying a large, unbiased sample of NEAs, is warranted.

We are indebted to the support teams of four telescopes and four instruments. We appreciate the help of Randy Campbell and Paola Amico with LWS at Keck I, Michael Ressler and Varoujan Gorjian in getting MIRLIN running at Keck II, Tom Kerr and Jane Buckle with Michelle at UKIRT, and Andrew Pickles with the UH 88 inch telescope and CCD cameras. The operation of MIRLIN is supported by an award from NASA's Office of Space Science. UKIRT is operated by the Joint Astronomy Centre on behalf of the UK Particle Physics and Astronomy Research Council. We thank telescope operators Joel Aycock, Meg Whittle, Wayne Wack, Tim Carroll, and John Dvorak. We acknowledge the JPL SSD group for their very useful "Horizons" ephemeris service and Ted Bowell for providing a comprehensive list of asteroid orbital elements. We thank the anonymous referee for helpful review. Discussions with Robert Jedicke, Petr Pravec, Audrey Delsanti, Olivier Groussin, Bin Yang, and Filip Hroch also improved this paper. This work was supported in part by grants to D. C. J. from NASA and by a SIRTF Fellowship to Y. R. F.

REFERENCES

Abell, P. A., et al. 2005, Icarus, in press
Allen, D. A. 1970, Nature, 227, 158
Bauer, J. M., Meech, K. J., Fernández, Y. R., Pittichova, J., Hainaut, O. R., Boehnhardt, H., & Delsanti, A. C. 2003, Icarus, 166, 195
Bell, J. F., Hawke, B. R., & Brown, R. H. 1988, Icarus, 73, 482
Benkhoff, J., & Huebner, W. F. 1996, Planet. Space Sci., 44, 1005
Benner, L. A. M., et al. 2002a, Icarus, 158, 379
Benner, L. A. M., et al. 2002b, Meteoritics Planet. Sci., 37, 779
Bottke, W. F., Morbidelli, A., Jedicke, R., Petit, J.-M., Levison, H. F., Michel, P., & Metcalfe, T. S. 2002, Icarus, 156, 399
Bowell, E., Hapke, B., Domingue, D., Lumme, K., Peltoniemi, J., & Harris, A. W. 1989, in Asteroids II, ed. R. P. Binzel et al. (Tucson: Univ. Arizona Press), 524
Bowell, E., et al. 1992, IAU Circ., 5585, 1
Brownlee, D. E., et al. 2004, Science, 304, 1764

Buratti, B. J., Hicks, M. D., Soderblom, L. A., Britt, D., Oberst, J., & Hillier, J. K. 2004, Icarus, 167, 16
Campins, H., & Fernández, Y. 2002, Earth Moon Planets, 89, 117
Cohen, M., Walker, R. G., Carter, B., Hammersley, P., Kidger, M., & Noguchi, K. 1999, AJ, 117, 1864
Cohen, M., Witteborn, F. C., Carbon, D. F., Davies, J. K., Wooden, D. H., & Bregman, J. D. 1996, AJ, 112, 2274
Cruikshank, D. P., & Jones, T. J. 1977, Icarus, 31, 427
Delbó, M., Harris, A. W., Binzel, R. P., Pravec, P., & Davies, J. K. 2003, Icarus, 166, 116
Engelke, C. W. 1992, AJ, 104, 1248
Fernández, J. A., Gallardo, T., & Brunini, A. 2002a, Icarus, 159, 358
Fernández, Y. R., Jewitt, D. C., & Sheppard, S. S. 2001, ApJ, 553, L197
———. 2002b, AJ, 123, 1050
Fernández, Y. R., Lisse, C. M., Käufl, H. U., Peschke, S. B., Weaver, H. A., Lamy, P. L., Livengood, T. A., & Kostiuk, T. 2000, Icarus, 147, 145
Fernández, Y. R., McFadden, L. A., Lisse, C. M., Helin, E. F., & Chamberlin, A. B. 1997, Icarus, 128, 114
Glasse, A. C. H., Atad-Ettedgui, E. I., & Harris, J. W. 1997, Proc. SPIE, 2871, 1197
Gradie, J. C., Chapman, C. R., & Tedesco, E. F. 1989, in Asteroids II, ed. R. P. Binzel et al. (Tucson: Univ. Arizona Press), 316
Green, S. F., Meadows, A. J., & Davies, J. K. 1985, MNRAS, 214, 29P
Harris, A. W. 1998, Icarus, 131, 291
Harris, A. W., & Davies, J. K. 1999, Icarus, 142, 464
Harris, A. W., Davies, J. K., & Green, S. F. 1998, Icarus, 135, 441
Harris, A. W., Delbó, M., Binzel, R. P., Davies, J. K., Roberts, J., Tholen, D. J., & Whiteley, R. J. 2001, Icarus, 153, 332
Harris, N. W., & Bailey, M. E. 1998, MNRAS, 297, 1227
Hartmann, W. K., Cruikshank, D. P., & Degewij, J. 1982, Icarus, 52, 377
Hartmann, W. K., Tholen, D. J., & Cruikshank, D. P. 1987, Icarus, 69, 33
Hoffmann, W. F., & Hora, J. L. 1999, MIRAC3 User's Manual (Tucson: Steward Obs.), http://cfa-www.harvard.edu/~jhora/mirac/mrcman.pdf
Hudson, R. S., & Ostro, S. J. 1995, Science, 270, 84
Jewitt, D. 2002, AJ, 123, 1039
———. 2005, AJ, 129, 530
Jewitt, D., & Sheppard, S. 2004, AJ, 127, 1784
Jones, B., & Puetter, R. 1993, Proc. SPIE, 1946, 610
Kührt, E., & Keller, H. U. 1994, Icarus, 109, 121
Lamy, P. L., Toth, I., Fernández, Y. R., & Weaver, H. A. 2004, in Comets II, ed. M. Festou, H. U. Keller, & H. A. Weaver (Tucson: Univ. Arizona Press), 223
Landolt, A. U. 1992, AJ, 104, 340
Lebofsky, L. A., Lebofsky, M. J., & Rieke, G. H. 1979, AJ, 84, 885
Lebofsky, L. A., & Spencer, J. S. 1989, in Asteroids II, ed. R. P. Binzel et al. (Tucson: Univ. Arizona Press), 128
Lebofsky, L. A., Veeder, G. J., Lebofsky, M. J., & Matson, D. L. 1978, Icarus, 35, 336
Lebofsky, L. A., et al. 1986, Icarus, 68, 239
Levison, H. F. 1996, in ASP Conf. Ser. 173, Completing the Inventory of the Solar System, ed. T. W. Rettig & J. M. Hahn (San Francisco: ASP), 173
Levison, H. F., & Duncan, M. J. 1994, Icarus, 108, 18
———. 1997, Icarus, 127, 13
Marsden, B. G., & Williams, G. V. 2003, Catalogue of Cometary Orbits 2003 (15th ed.; Cambridge: SAO)
Matson, D. K. 1972, Ph.D. thesis, California Inst. Technol.
Morbidelli, A., Jedicke, R., Bottke, W. F., Michel, P., & Tedesco, E. F. 2002, Icarus, 158, 329
Morrison, D. 1973, Icarus, 19, 1
Morrison, D., Gradie, J. C., & Rieke, G. H. 1976, Nature, 260, 691
Mottola, S., et al. 1997, AJ, 114, 1234
Müller, T. G., Sterzik, M. F., Schütz, O., Pravec, P., & Siebenmorgen, R. 2004, A&A, 424, 1075
Öpik, E. J. 1963, Irish Astron. J., 6, 93
Pravec, P., Wolf, M., Sarounova, L., Harris, A. W., & Davies, J. K. 1997, Icarus, 127, 441
Ressler, M. E., Werner, M. W., Van Cleve, J., & Chou, H. A. 1994, Exp. Astron., 3, 277
Rickman, H., Fernández, J. A., & Gustafson, B. Å. S. 1990, A&A, 237, 524
Schaefer, B. E., & Rabinowitz, D. L. 2002, Icarus, 160, 52
Sekiguchi, T., Abe, M., Boehnhardt, H., Dermawan, B., Hainaut, O. R., & Hasegawa, S. 2003, A&A, 397, 325
Sheppard, S. S., & Jewitt, D. C. 2002, AJ, 124, 1757
Stansberry, J. A., et al. 2004, ApJS, 154, 463
Tedesco, E. F., ed. 1992, *IRAS* Minor Planet Survey (Phillips Lab. Tech. Rep. PL-TR-92-2049) (Hanscom AFB, MA: Phillips Lab., Dir. Geophys., Air Force Mater. Command)
Tedesco, E. F., & Gradie, J. 1987, AJ, 93, 738
Tedesco, E. F., Noah, P. V., Noah, M., & Price, S. D. 2002, AJ, 123, 1056
Tisserand, F. 1896, Traité de Mécanique Céleste, Vol. 4 (Paris: Gauthier-Villars)
Tokunaga, A. 1984, AJ, 89, 172
Veeder, G. J., Hanner, M. S., Matson, D. L., Tedesco, E. F., Lebofsky, L. A., & Tokunaga, A. T. 1989, AJ, 97, 1211
Wetherill, G. W. 1979, Icarus, 37, 96
Whiteley, R. J., Tholen, D. J., & Hergenrother, C. W. 2002, Icarus, 157, 139
Yang, B., Zhu, J., Gao, J., Ma, J., Zhou, X., Wu, H., & Guan, M. 2003, AJ, 126, 1086